Polytypism in mcalpineite: a study of natural and synthetic Cu_3TeO_6

Owen P. Missen,[a,b]* Stuart J. Mills,[b] Stefano Canossa,[c] Joke Hadermann,[c] Gwilherm Nénert,[d] Matthias Weil,[e] Eugen Libowitzky,[f] Robert M. Housley,[g] Werner Artner,[h] Anthony R. Kampf,[i] Michael S. Rumsey,[j] John Spratt,[k] Koichi Momma[l] and Maja A. Dunstan[m]

[a]School of Earth, Atmosphere and Environment, Monash University, 9 Rainforest Walk, Clayton 3800, Victoria, Australia, [b]Geosciences, Museums Victoria, GPO Box 666, Melbourne 3001, Victoria, Australia, [c]EMAT, Department of Physics, University of Antwerp, Groenenborgerlaan 171, 2020 Antwerpen, Belgium, [d]Malvern Panalytical B.V., Lelyweg 1, 7602 EA Almelo, The Netherlands, [e]Institute for Chemical Technologies and Analytics, Division of Structural Chemistry, TU Wien, Getreidemarkt 9/164-SC, A-1060 Vienna, Austria, [f]Institute for Mineralogy and Crystallography, Faculty of Geosciences, Geography and Astronomy, Universität Wien, Althanstr. 14, A-1090 Vienna, Austria, [g]Division of Geological and Planetary Sciences, California Institute of Technology, Pasadena, CA 91125, USA, [h]X-ray Center, TU Wien, Getreidemarkt 9, A-1060 Vienna, Austria, [i]Mineral Sciences Department, Natural History Museum of Los Angeles County, 900 Exposition Boulevard, Los Angeles, CA 90007, USA, [j]Department of Earth Sciences, Natural History Museum, Cromwell Road, London, SW7 5BD, UK, [k]Core Research Laboratories, Natural History Museum, 21 Cromwell Road, London, UK, SW7 5BD, [l]National Museum of Nature and Science, 4-1-1 Amakubo, Tsukuba, Ibaraki 305-0005, Japan, and [m]School of Chemistry, University of Melbourne, Parkville, Victoria, 3010, Australia. *Correspondence e-mail: omissen@museum.vic.gov.au

Synthetic and naturally occurring forms of tricopper orthotellurate, $Cu^{II}_3Te^{VI}O_6$ (the mineral mcalpineite) have been investigated by 3D electron diffraction (3D ED), X-ray powder diffraction (XRPD), Raman and infrared (IR) spectroscopic measurements. As a result of the diffraction analyses, $Cu^{II}_3Te^{VI}O_6$ is shown to occur in two polytypes. The higher-symmetric $Cu^{II}_3Te^{VI}O_6$-1C polytype is cubic, space group $Ia\bar{3}$, with a = 9.537 (1) Å and V = 867.4 (3) Å^3 as reported in previous studies. The 1C polytype is a well characterized structure consisting of alternating layers of $Cu^{II}O_6$ octahedra and both $Cu^{II}O_6$ and $Te^{VI}O_6$ octahedra in a patchwork arrangement. The structure of the lower-symmetric orthorhombic $Cu^{II}_3Te^{VI}O_6$-2O polytype was determined for the first time in this study by 3D ED and verified by Rietveld refinement. The 2O polytype crystallizes in space group $Pcca$, with a = 9.745 (3) Å, b = 9.749 (2) Å, c = 9.771 (2) Å and V = 928.3 (4) Å^3. High-precision XRPD data were also collected on $Cu^{II}_3Te^{VI}O_6$-2O to verify the lower-symmetric structure by performing a Rietveld refinement. The resultant structure is identical to that determined by 3D ED, with unit-cell parameters a = 9.56157 (19) Å, b = 9.55853 (11) Å, c = 9.62891 (15) Å and V = 880.03 (2) Å^3. The lower symmetry of the 2O polytype is a consequence of a different cation ordering arrangement, which involves the movement of every second $Cu^{II}O_6$ and $Te^{VI}O_6$ octahedral layer by (1/4, 1/4, 0), leading to an offset of $Te^{VI}O_6$ and $Cu^{II}O_6$ octahedra in every second layer giving an $ABAB*$ stacking arrangement. Syntheses of $Cu^{II}_3Te^{VI}O_6$ showed that low-temperature (473 K) hydrothermal conditions generally produce the 2O polytype. XRPD measurements in combination with Raman spectroscopic analysis showed that most natural mcalpineite is the orthorhombic 2O polytype. Both XRPD and Raman spectroscopy measurements may be used to differentiate between the two polytypes of $Cu^{II}_3Te^{VI}O_6$. In Raman spectroscopy, $Cu^{II}_3Te^{VI}O_6$-1C has a single strong band around 730 cm^{-1}, whereas $Cu^{II}_3Te^{VI}O_6$-2O shows a broad double maximum with bands centred around 692 and 742 cm^{-1}.

1. Introduction

$Cu^{II}_3Te^{VI}O_6$ was first studied as a synthetic compound by Hostachy & Coing-Boyat (1968) and subsequently by Falck *et al.* (1978). They both determined the crystal structure in the cubic space group $Ia\bar{3}$. Hostachy & Coing-Boyat (1968)
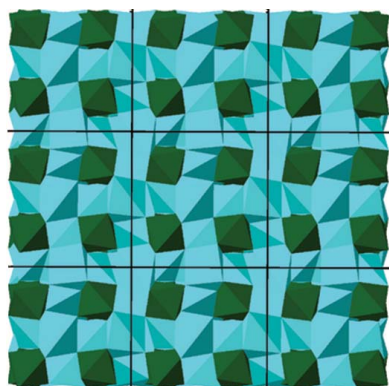
synthesized $Cu^{II}_3Te^{VI}O_6$ in a solid-state reaction of $CuCO_3$ and $Te(OH)_6$, heated at 973 K in air for 36 h, while Falck *et al.* (1978) synthesized their $Cu^{II}_3Te^{VI}O_6$ crystals at high-temperature (973 K) and under high-pressure (900 bar) hydrothermal conditions for one week using aqueous solutions of $CuSO_4$ and H_6TeO_6. Subsequently, $Cu^{II}_3Te^{VI}O_6 \cdot H_2O$ was described as a mineral in 1994 by Roberts *et al.* (1994) and given the name mcalpineite. More recently, synthetic $Cu^{II}_3Te^{VI}O_6$ has been widely studied for its three-dimensional antiferromagnetic properties (*e.g.* Herak *et al.*, 2005; Choi *et al.*, 2008; Zhu *et al.*, 2014; Chakraborty, 2019; Wang *et al.*, 2019), while copper tellurium oxides in general are of interest for their magnetic properties (Norman, 2016, 2018; Inosov, 2018). Recently, we undertook a study to generate synthetic analogues of rare copper(II) tellurate minerals without known crystal structures, such as brumadoite $[Cu_3(Te^{VI}O_4)-(OH)_4 \cdot 5H_2O$; Atencio *et al.* (2008)] and xocomecatlite $[Cu_3(Te^{VI}O_4)(OH)_4$; Williams (1975)]. These experiments tended to produce phases with X-ray powder diffraction (XRPD) patterns similar to $Cu^{II}_3Te^{VI}O_6$, indicating the stability of phases with this formula. Our interest was piqued by the presence of additional minor XRPD reflections in the low-temperature (423–473 K) hydrothermally grown $Cu^{II}_3Te^{VI}O_6$, which did not match the synthetic patterns for *I*-centred cubic $Cu^{II}_3Te^{VI}O_6$, but were a good match for mcalpineite (Roberts *et al.*, 1994).

Roberts *et al.* (1994) reported mcalpineite as copper tellurate monohydrate, $Cu^{II}_3Te^{VI}O_6 \cdot H_2O$, in a primitive unit-cell but otherwise undetermined cubic space group. This phase was first reported from two cotype localities: the McAlpine mine, California, USA (37°45′58″N, 120°15′9″W) and the Centennial Eureka mine, Utah, USA (39°56′36″N, 112°7′19″). The latter mine is the type locality for six other Cu-containing Te oxysalt minerals: eurekadumpite $[(Cu,Zn)_{16}(Te^{IV}O_3)_2-(AsO_4)_3Cl(OH)_{18} \cdot 7H_2O$; Pekov *et al.* (2011)], frankhawthorneite $[Cu_2Te^{VI}O_4(OH)_2$; Roberts *et al.* (1995)], jensenite $[Cu_3Te^{6+}O_6 \cdot 2H_2O$; Roberts *et al.* (1996*a*)], juabite $[CaCu_{10}(Te^{IV}O_3)_4(AsO_4)_4(OH)_2 \cdot 4H_2O$; Roberts, Gault *et al.* (1997)], leisingite $[Cu_2MgTe^{VI}O_6 \cdot 6H_2O$; Roberts *et al.* (1996*b*)] and utahite $[MgCu_4Zn_2Te^{VI}_3O_{14}(OH)_4 \cdot 6H_2O$; Roberts, Stirling *et al.* (1997*b*)]. The specimen from the Centennial Eureka Mine was used for H_2O determination by Roberts *et al.* (1994). No crystal structure was reported for mcalpineite, although crystallization in a cubic space group with a primitive lattice (exact symmetry unknown) was reported. Roberts *et al.* (1994) also noted the similarity to synthetic $Cu^{II}_3Te^{VI}O_6$, noting a 4 Å void with 'marginally sufficient room' to incorporate an H_2O molecule as indicated in the formula $Cu^{II}_3Te^{VI}O_6 \cdot H_2O$. A subsequent study on mcalpineite from the Gambatesa mine in Italy, along with a synthetic sample of $Cu^{II}_3Te^{VI}O_6$ generated from binary oxides at high temperature, led to the redefinition of the species as anhydrous $Cu^{II}_3Te^{VI}O_6$ (Carbone *et al.*, 2013). Carbone *et al.* (2013) used powder X-ray diffraction, electron diffraction and Raman spectroscopic measurements to redefine mcalpineite in space group $Ia\bar{3}$, *i.e.* as identical to synthetic *I*-centred $Cu^{II}_3Te^{VI}O_6$. Carbone *et al.* (2013) concluded that the extra

lines in the powder X-ray diffraction pattern of their natural mcalpineite sample [*i.e.* those contributing to the primitive unit cell described by Roberts *et al.* (1994)] were from an unidentified associated phase, rather than a $Cu^{II}_3Te^{VI}O_6$ phase.

While generally rare, Te—O minerals are a rich source of new and rare structures, increasingly solved through a combination of Rietveld refinement with a structural refinement due to the ever-decreasing crystal size of Te—O minerals without a known structure (Nénert *et al.*, 2020). While rare and polycrystalline, mcalpineite is now known to be far more common in Nature than when first discovered. It is prevalent at the Otto Mountain mines, California, where it forms early in the secondary mineral paragenetic sequence and is usually found as grass green coatings on rocks hosting suites of unique, rare secondary Te minerals (Housley *et al.*, 2011; Christy *et al.*, 2016*a*). Here, we present data on the structure and occurrence of the two polytypes of $Cu^{II}_3Te^{VI}O_6$, including assigning polytypes for well characterized mcalpineite occurrences.

2. Experimental

Descriptions of the syntheses of the $Cu^{II}_3Te^{VI}O_6$ polytypes and the provenance of the natural mcalpineite samples are summarized in the following two sections and in Table 1.

Figure 1
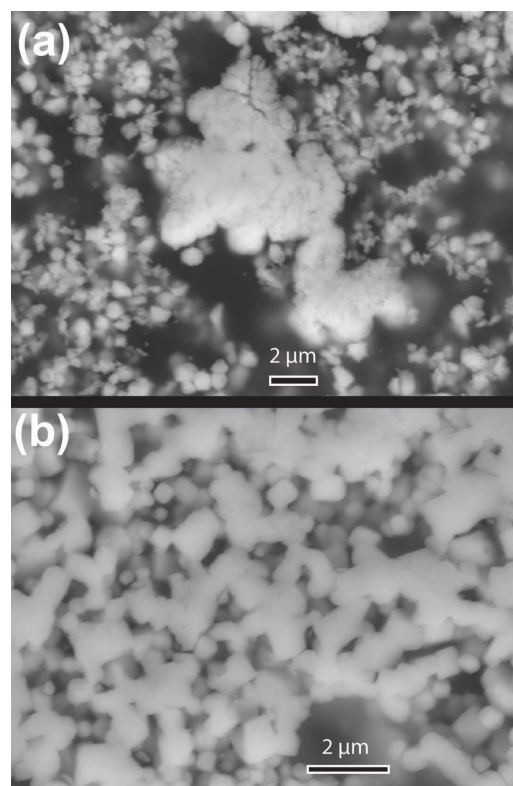SEM images (backscatter electron mode) of synthetic $Cu^{II}_3Te^{VI}O_6$-2O (*a*) and $Cu^{II}_3Te^{VI}O_6$-1C from solid state synthesis (*b*), showing 0.5 µm prisms and 20 µm polycrystalline aggregates of the 2O polytype and 0.3–1.5 µm cubes for the 1C polytype.

Table 1
Sample summary incorporating details of natural mcalpineite samples and synthetic $Cu^{II}_3Te^{VI}O_6$ samples analysed in this study.

Syn or nat	Polytype	Locality	Synthesis detail	XRPD	SEM or EPMA	IR or Raman
Natural	2O	BND[1]	NA	Yes	SEM	Raman
Natural	2O	Aga[2]	NA	Yes	SEM	Raman
Natural	2O	Serita[3]	NA	Yes	Neither	Raman
Natural	2O	CEM[4]	NA	Yes	SEM	Raman
Natural	2O	RM[5]	NA	Yes	Neither	Neither
Natural	2O	Delamar[6]	NA	Yes	SEM	Raman
Natural	2O	Wildcat[7]	NA	No	Neither	Raman
Natural	2O	Norway[8]	NA	Yes	EPMA	Neither
Synthetic	2O	NA	Hydrothermal	Yes	SEM	Both
Synthetic	1C	NA	Solid state	Yes	SEM	IR
Synthetic	1C	NA	CVT	Yes	Neither	Both

(1) Bird Nest drift, Otto Mountain, California, USA (35°16′36″N, 116°6′0″W); (2) Aga mine, Otto Mountain, California, USA (35°16′19″N, 116°5′42″W); (3) Serita mine, Masonic Mountain, California, USA (38°21′35″N, 119°7′35″W); (4) Centennial Eureka mine, Utah, USA (39°56′36″N, 112°7′19″W); (5) Reef mine, Sierra Vista, Arizona, USA (31°25′37″N, 110°17′16″W); (6) Delamar mine, Delamar district, Nevada, USA (37°27′43″N, 114°46′7″W); (7) Wildcat prospect, Utah, USA (39°35′34″N, 113°6′58″W); (8) Millsite Boulder, Gråurdfjellet, Norway (62°29′11″N, 9°29′25″E), specimen number BM 2011,243 (Natural History Museum, London).

Table 2
Summary of synthetic $Cu^{II}_3Te^{VI}O_6$ in literature studies.

Reference	Polytype (if determinable)	Synthesis method	Synthesis temperature (K)	PD	SEM	IR or Raman	Study aim
Herak et al. (2005)	1C	CVT	723–773 or 823–873	Yes, neutron	No	No	Magnetic properties
Choi et al. (2008)	1C	CVT	Unstated	No	No	Raman	Magnetic properties
Zhu et al. (2014)	1C	Sintering or calcination	1138 or 1123, respectively	Yes, X-ray	Yes	No	Ceramic dielectrics
He & Itoh (2014)	1C	Solid state	1223	Yes, X-ray	No	No	Magnetic properties
Mutharani et al. (2020)	1C	Precipitation then calcination	Calcination at 873	Yes, X-ray	Yes	No	Ibuprofen sensing

2.1. Synthesis

Three methods were employed for synthesis of $Cu^{II}_3Te^{VI}O_6$ in this study: low-temperature hydrothermal synthesis, high-temperature solid-state synthesis and chemical vapour transport (CVT), the latter used to grow $Cu^{II}_3Te^{VI}O_6$ crystals from material synthesized by the solid-state method. The archetypical synthetic samples used for most measurements are summarized in Table 1 and a summary of $Cu^{II}_3Te^{VI}O_6$ syntheses in other studies is provided in Table 2. Scanning electron micrographs of the synthetic $Cu^{II}_3Te^{VI}O_6$ polytypes were taken on a JEOL 7001 F FEG-SEM (20 kV, 3 nA and 2 µm beam diameter) at the Monash Centre for Electron Microscopy, Monash University, Australia (Fig. 1).

Hydrothermal synthesis of $Cu^{II}_3Te^{VI}O_6$ was carried out in two batches of experiments. The first batch of experiments at Museums Victoria used the following Cu^{II} compounds as starting materials: CuO, $Cu_2(CO_3)(OH)_2$ and $Cu(NO_3)_2\cdot3H_2O$, including $Cu(NO_3)_2\cdot3H_2O$ in combination with both other Cu^{II} compounds. $Te(OH)_6$ and TeO_2 (the latter oxidized in situ) were used as the Te sources. The starting materials were added to 25 ml Teflon-lined steel vessels, then filled to 10 ml with water. These vessels were added to hand-tightened steel autoclaves and heated to 473 K for a period of 3–7 days, followed by furnace cooling. Hand-tightening allowed for more rapid evaporation of H_2O, and the products obtained were dry.

The second batch of experiments at TU Wien used $Cu(OH)_2$, $Cu(NO_3)_2\cdot2.5H_2O$, $CuSO_4\cdot5H_2O$ or $CuCl_2\cdot2H_2O$ as Cu^{II} sources. $Te(OH)_6$ was most commonly used as the Te^{VI} source, with $KTeO(OH)_5$ used as an occasional alternative.

The reagents were added to Teflon-lined steel vessels (maximum capacity 7 ml) which were filled with water to an approximate two-thirds loading, then sealed in steel autoclaves via mechanical tightening and heated at autogenous pressure at 473 K for 2–11 days, followed by furnace cooling. The resultant contents of the Teflon vessels were filtered through a Büchner funnel, washing the solid products with mother liquor, then deionized water, ethanol and acetone, followed by drying in air. A 3:1 molar ratio of Cu^{II}:Te^{VI} was
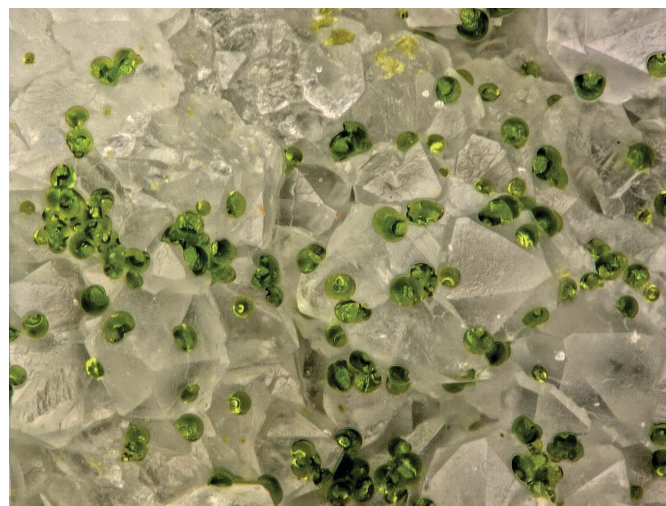

Figure 2
Natural mcalpineite-2O from Bird Nest drift, Otto Mountain as grass-green spherules on quartz, FOV 0.56 mm. Natural History Museum of Los Angeles County specimen number 69339.

usually employed but other ratios were used on occasion when attempting to synthesize different Cu^{II}–Te^{VI} minerals.

Solid-state synthesis of $Cu^{II}_3Te^{VI}O_6$ employed a Cu^{II} compound, either $Cu(OH)_2$ or $Cu(NO_3)_2 \cdot 2.5H_2O$ with $Te(OH)_6$, again in a 3:1 molar ratio. The reactants were weighed out and ground together in a mortar and pestle. Following initial heating to 673 K in a ceramic crucible over 2 h, the reaction mixture (as black powder) was removed from the furnace and reground, then returned to the crucible and heated to the final reaction temperature of 873 K over the course of 1 hour. The crucible was maintained at 873 K for 24 h then cooled to room temperature over 5 h, producing a grass-green powder.

CVT-based crystal growth (Binnewies et al., 2012) of $Cu^{II}_3Te^{VI}O_6$ used previously solid-state synthesized $Cu^{II}_3Te^{VI}O_6$ polycrystalline powders, with a 10:1 mass ratio of $Cu^{II}_3Te^{VI}O_6$ with the Cl_2 source, $PtCl_2$. The reagents (overall load ca 0.2 g) were ground together with a mortar and pestle, then vacuum-sealed in a silica glass ampoule and placed in a temperature gradient furnace for a period of two weeks. The temperature was set at 1023 K at the source end and 953 K at the sink end. Amorphous green material was produced on top of bubbled glass, indicating attack of the glass surface by the reagents. Dark-green, well faceted octahedral crystals of $Cu^{II}_3Te^{VI}O_6$ were grown in the sink end of the glass ampoule, with no other crystalline phases detected.

2.2. Sample details

Natural mcalpineite samples from seven localities were analysed, with summary details shown in Table 1. In almost all cases, mcalpineite forms grass-green coatings, occasionally botryoidal in nature, on quartz (Fig. 2) or as polycrystalline crusts. Well formed single crystals of mcalpineite (micron-scale dimensions) are so far not known in Nature. Mcalpineite from the Millsite Boulder, Gråurdfjellet, Norway (62°29′11″N, 9°29′25″E; Rumsey et al., 2018) forms a botryoidal dark-olive-green to black crust with no visible crystallinity. Despite the darker visual appearance, the streak is bright green, typical of mcalpineite.

2.3. 3D electron diffraction

Three-dimensional electron diffraction (3D ED) series from a $10 \times 15 \times 20$ nm single crystal were acquired on a FEI Titan 'cubed' microscope operated at 300 kV. 3D ED is becoming a more prominent tool in inorganic chemistry as it allows for the analysis of nanocrystals (Kolb et al., 2007; Gemmi et al., 2019).

The sample was prepared for the analysis by manually grinding the powder in an agate mortar, recovering the resulting powder with ethanol, and sonicating the resulting suspension for 10 min at room temperature. The thus-obtained suspension was appropriately diluted with ethanol and used to deposit one droplet on a copper grid for TEM analysis. The sample grid was loaded on a Fischione2020 tomography holder, and inserted in the TEM column at room temperature without further treatment. The electron beam was adjusted using spot size No. 9 ($\sim$190 nm beam size at the sample), and

condenser apertures C1, C2, and C3 of 2000 µm, 50 µm and 2000 µm, respectively, while a selected aperture was used to selectively illuminate the sample during data acquisition. Static ED patterns were collected every 0.5°, covering a range of 140° by using custom-made script for Digital Micrograph for stepwise ED data acquisition, while the camera length was set at 285 mm. Data integration was conducted by using the software PETS2.0 using an integration range of 0.25–1.25 Å^{-1} (Palatinus et al., 2019), while for structure solution and refinement by the charge-flipping method, the programs Superflip (Palatinus & Chapuis, 2007) and Refine (least-squares) were used within the software Jana2020 (Petříček et al., 2014). Note that the low number of reflections used for indexing is due to the presence of a minor twin domain in the data. This did not create noteworthy problems in the indexing and refinement of the unit-cell, nor did it affect the reciprocal space reconstructions. However, to avoid the presence of this parasitic domain in the peak table used for unit-cell determination, we used an intensity threshold that filtered out the weakest reflections, thus effectively decreasing their number compared to the total number of observed reflections.

The crystal structure refined by 3D ED data can be accessed free of charge from the joint CCDC and FIZ Karlsruhe's access service WebCSD (https://www.ccdc.cam.ac.uk/structures/) by entering the reference code CSD2110654.

2.4. X-ray powder diffraction

2.4.1. Fingerprint scans. Fingerprint X-ray powder diffraction (XRPD) scans were performed on a Philips X'Pert diffractometer, Museums Victoria, Australia, using Cu $K\alpha$ radiation (40 kV and 40 mA) for the pilot-project hydrothermal syntheses. All subsequent $Cu^{II}_3Te^{VI}O_6$ samples were synthesized at TU Wien, in which case representative samples of the bulk products were ground, fixed with small amounts of petroleum jelly on zero-background silicon wafers and measured with Cu $K\alpha_{1,2}$ radiation in Bragg–Brentano geometry on a PANalytical X'PertPro system. Example XRPD scans of synthetic $Cu^{II}_3Te^{VI}O_6$-1C and $Cu^{II}_3Te^{VI}O_6$-2O are shown in Fig. 3.
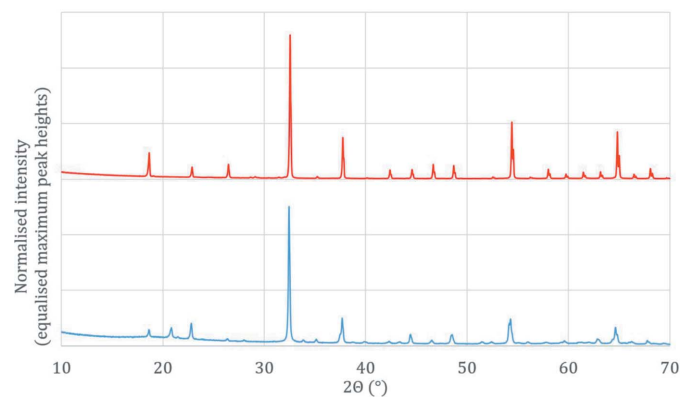
Figure 3
Representative XRPD scans collected using Cu $K\alpha$ of both $Cu^{II}_3Te^{VI}O_6$-1C (above, red) and $Cu^{II}_3Te^{VI}O_6$-2O (below, blue) polytypes of synthetic $Cu^{II}_3Te^{VI}O_6$. Scans normalized to the height of the maximum peak.

Table 3
ED and Rietveld structural refinement details of $Cu^{II}_3Te^{VI}O_6$-2O.

Crystal data	ED	Rietveld
Ideal chemical formula	$Cu^{II}_3Te^{VI}O_6$	$Cu^{II}_3Te^{VI}O_6$
Crystal system, space group	Orthorhombic, *Pcca*	Orthorhombic, *Pcca*
Temperature (K)	293	293
a, b, c (Å)	9.745 (3), 9.749 (2), 9.771 (2)	9.56156 (19), 9.55853 (11), 9.62891 (15)
V (Å^3)	928.3 (4)	880.03 (2)
Z	8	8
Calculated density (g cm^{-3})	5.928	6.253
Radiation type and wavelength λ (Å)	Electron, 0.0197	X-ray (Mo), 0.70932
Crystal dimensions (nm)	$10 \times 15 \times 20$	$20 \times 13.5 \times 64.5$
No. of reflections	206	3964
Angle range (°) for cell refinement	0.12–0.71	4–70
Data collection		
Description	Irregular green	Light-green powder
Diffractometer	US1000 CCD detector	PANalytical Empyrean
θ (°) range	0.232–1.410	4–70
Indices range of h, k, l	−12 to 12 for all indices	0 to 15 for all indices
No. of measured, independent and observed [$I > 3\sigma(I)$] reflections	4206, 935, 631	3964
R_{int}, R_{sigma}	0.1649, 0.0183	NA
Data completeness to 0.71°θ (%)	99	NA
Refinement		
Number of reflections, parameters, restraints	935, 96, 0	3964, 73, 0
$R_1[F^2 > 2\sigma(F^2)]$, R_1(all)	0.1410, 0.1841	NA
R_{wp} (Rietveld)	NA	0.0255
$wR_2[F^2 > 2\sigma(F^2)]$, wR_2(all)	0.2946, 0.3026	NA
GoF (F^2)	6.5501	NA

The majority of XRPD scans on natural samples were collected on a Rigaku R-Axis Rapid II curved imaging plate diffractometer using Mo $K\alpha$ radiation at the Natural History Museum of Los Angeles County and a dataset collected using Mo $K\alpha$ radiation to 32° 2θ. The only exception was the XRPD scan for the Norway sample, collected on a Rigaku R-Axis Rapid II diffractometer at the Natural History Museum, London, with a dataset collected using Cu $K\alpha$ radiation to 80° / 2θ.
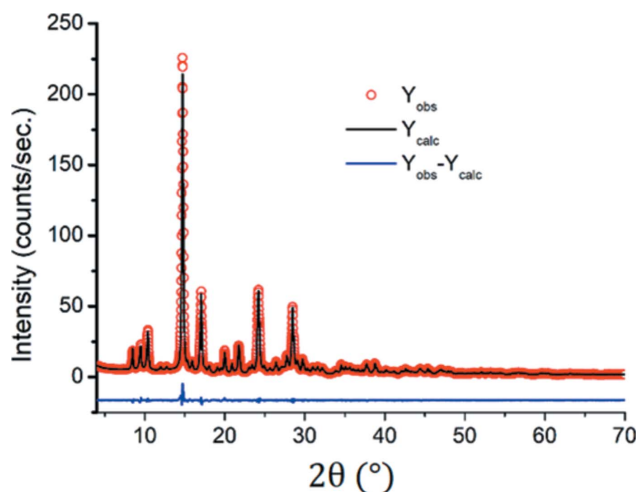

Figure 4
Rietveld refinement of $Cu^{II}_3Te^{VI}O_6$-2O collected with Mo radiation (R_{wp} = 2.55%).

2.4.2. Rietveld refinement. For high-resolution Rietveld refinement, a XRPD scan of synthetic $Cu^{II}_3Te^{VI}O_6$-2O was undertaken (Fig. 4). To ensure a totally random orientation for XRPD analysis, the sample powder was loaded into borosilicate glass capillary tubes (external diameter 0.5 mm, wall thickness 0.01 mm). XRD analysis was carried out at room temperature using a PANalytical Empyrean diffractometer with a Debye–Scherrer geometry. For optimal data collection, hard radiation was used (high-resolution Mo tube) with an incident beam focusing mirror and a GalPIX^{3D} detector. The capillary was rotated at a speed of 5 revolutions/s and scans performed in the range 2θ = 4–70° with a step size of 0.014°. A variable counting time strategy was employed to increase the counting statistics (refinement details shown in Table 3).

2.4.3. *In situ* XRPD. *In situ* XRPD scans were performed under atmospheric conditions on a HTK1200 Anton-Paar high-temperature oven chamber using a Philips X'Pert diffractometer at TU Wien. The sample used was hydrothermally synthesized $Cu^{II}_3Te^{VI}O_6$-2O. The sample was loaded into a corundum sample holder and held at 298 K for 10 minutes then at 348 K for 2.5 h to drive off any remaining moisture. Heating was performed at a rate of 60 K h^{-1}, with a powder diffraction scan recorded every 5 K. The temperature remained constant during the scan time. Scans were recorded from 298 K to 873 K, with an additional scan collected following cooling back to 303 K.

2.4.4. Raman spectroscopy. Raman spectra on synthetic samples (Fig. 5) were collected at Universität Wien on a Renishaw RM1000 confocal edge filter-based micro-Raman system. The 488 nm excitation line of a $\sim$20 mW Ar-ion laser

was focused with a 50×/0.75 objective lens on the sample surface. The back-scattered radiation (180° configuration) was analysed with a 1200 lines/mm grating monochromator. Raman intensities were collected for 30 s (spectral range 4000 to ~70 cm^{-1} in continuous grating scan mode) with a thermo-electrically cooled CCD array detector. The spectral resolution of the system was 5−6 cm^{-1}, the wavenumber accuracy was 1 cm^{-1} (both calibrated with the Rayleigh line and the 521 cm^{-1} line of a Si standard). The confocal setup limited the spatial (lateral and depth) resolution to 2−3 µm. Instrument control and data acquisition were done with Grams/32 software (Galactic Ind. Corp.). Raman spectra on CVT-produced $Cu^{II}_3Te^{VI}O_6$ were collected for 120 s using full laser power. Hydrothermally produced $Cu^{II}_3Te^{VI}O_6$ was visibly burnt at full laser power, hence spectra were collected for 120 s with laser power attenuated to 10%. No features were observed between 4000 and 1100 cm^{-1} for either specimen.

Raman spectra on two mcalpineite specimens from Bird Nest drift at Otto Mountain were collected at Caltech, also on

Figure 5
Representative Raman spectra of the synthetic $Cu^{II}_3Te^{VI}O_6$-1C polytype synthesized by CVT (orange), synthetic hydrothermal $Cu^{II}_3Te^{VI}O_6$-2O polytype (blue) and a natural sample from Bird Nest drift, Otto Mountain, California (green – note that a different instrument was used, with a 170 cm^{-1} cut-off) with key vibration lines labelled.

Figure 6
Representative IR spectra of the $Cu^{II}_3Te^{VI}O_6$-1C synthesized by CVT (orange), synthetic $Cu^{II}_3Te^{VI}O_6$-1C synthesized by solid-state reaction (red) and hydrothermal $Cu^{II}_3Te^{VI}O_6$-2O (blue) key vibration lines labelled.

a Renishaw RM1000 spectrometer but this time with a 514 nm solid-state laser (Fig. 5). Most scanning was done at 10% power and 20× magnification resulting in a 5 µm spot size, collecting a spectral range of 1600 to ~170 cm^{-1} in continuous grating scan mode. A polarization scrambler was used to minimize polarization effects and the energy scale was also calibrated with silicon. Other details are as above for the synthetic samples.

2.5. IR spectroscopy

IR spectra of the two polytypes (Fig. 6) were collected from 4000 to 370 cm^{-1} on a Bruker TENSOR 27 Fourier-transform infrared (FTIR) spectrometer equipped with a HARRICK MVP2 diamond attenuated total reflectance (ATR) unit at Universität Wien. A glowbar lightsource, a KBr beam splitter, and a DLaTGS detector were used. Each 32 spectra, with a resolution of 4 cm^{-1}, were averaged for a good signal-to-noise ratio both for reference (from the empty ATR unit) and sample spectra. Instrument control and data handling was done with Bruker *OPUS 5.5* software.

2.6. Thermal analysis

Differential scanning calorimetry (DSC) measurements were performed under flowing argon atmosphere (10 ml min^{-1}) on a Netzsch DSC 200 F3 at TU Wien, using a ~10 mg dried sample of powdered, synthetic $Cu^{II}_3Te^{VI}O_6$-2O.

Thermogravimetric analysis (TGA) measurements were performed under flowing argon atmosphere (10 ml min^{-1}) on a Netzsch TG 209 T3 at TU Wien, again using a ~10 mg dried sample of powdered, synthetic $Cu^{II}_3Te^{VI}O_6$-2O.

2.7. Electron probe micro-analysis

Quantitative chemical analyses of mcalpineite, sample BM 2011,243 from Millsite Boulder, Gråurdfjellet, Norway, were performed on a Cameca SX100 Electron Microprobe (WDS mode, 12 kV, 10 nA, 5 µm beam diameter and PAP matrix correction) at the Imaging and Analysis Centre, Core Research Laboratories, Natural History Museum, London. Fe_2O_3, CuO, TeO_3 and UO_2 were analysed, with Fe_2O_3 totals not exceeding 0.1 wt%. CaO and As_2O_5 were also sought, but not detected. No other elements were detected using energy dispersive X-ray spectroscopy or electron probe micro-analysis (EPMA) and as a known anhydrous mineral there was no need to calculate H_2O.

3. Results and discussion

3.1. Crystal structure of the polytypes

3.1.1. $Cu^{II}_3Te^{VI}O_6$-1C. $Cu^{II}_3Te^{VI}O_6$-1C has a bixbyite-like structure (Fig. 7) consisting of $Cu^{II}O_6$ and $Te^{VI}O_6$ octahedra as revealed by one previous single-crystal X-ray diffraction study (Falck *et al.*, 1978) and two Rietveld refinements (Hostachy & Coing-Boyat, 1968; Carbone *et al.*, 2013). $Cu^{II}_3Te^{VI}O_6$-1C (space group $Ia\bar{3}$), has only three distinct sites: one Cu (multiplicity 24, Wyckoff letter d, site symmetry 2..), one Te
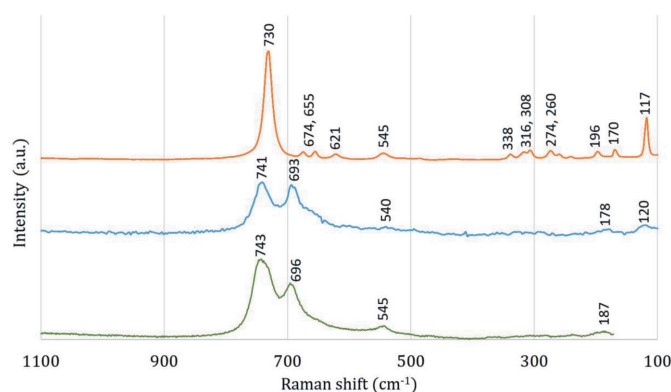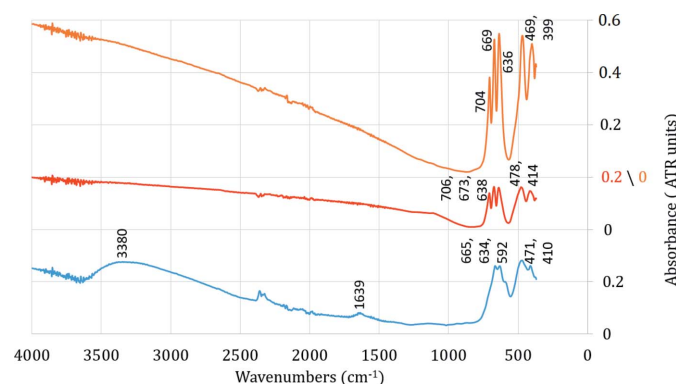
(8*b*, .$\bar{3}$.), and one O (48*e*, 1) site. The $Cu^{II}O_6$ octahedra form a three-dimensional framework *via* both edge- and corner-sharing. Cu–O bond lengths are 2 × 1.949 (2) Å and 2 × 2.031 (3) Å for equatorial bond lengths and 2 × 2.369 (3) Å for axial bond lengths (Falck *et al.*, 1978). These $Cu^{II}O_6$ octahedra are asymmetric as well as Jahn–Teller distorted, with a O_{axial}—Cu—O_{axial} angle of ~133°, while $Te^{VI}O_6$ octahedra are symmetrical with six Te—O bonds at 1.921 (2) Å. The $Te^{VI}O_6$ octahedra are isolated from each other and are linked into the {Cu–O} framework *via* edge-sharing with $Cu^{II}O_6$ octahedra (Christy *et al.*, 2016*b*). The remaining void space in the structure is not large enough to incorporate a H_2O molecule without significant rearrangement of the framework (Carbone *et al.*, 2013).

3.1.2. $Cu^{II}_3Te^{VI}O_6$-2*O*. The crystal structure of $Cu^{II}_3Te^{VI}O_6$-2*O* has been first determined during the current study by 3D ED. The *Pcca* space group was assigned upon observation, in reciprocal space reconstructions of the main zones, of the corresponding extinction rules [*l* = 2*n* in (0*kl*) and

(*h*0*l*), *h* = 2*n* in (*hk*0); Fig. 8]. After structure solution and refinement, the final structure was checked for compatible higher space-group symmetry by the ADDSYM tool of the program *PLATON* (Spek, 2020), which did not find any suitable alternative setting. $Cu^{II}_3Te^{VI}O_6$-2*O* contains the same octahedral building blocks as $Cu^{II}_3Te^{VI}O_6$-1*C*, however the octahedral layers contain a different stacking arrangement (Fig. 7). The lower symmetry of the 2*O* polytype is generated by the movement of every second $Cu^{II}O_6$ and $Te^{VI}O_6$ octahedral layer by (1/4, 1/4, 0), leading to an offset of $Te^{VI}O_6$ and
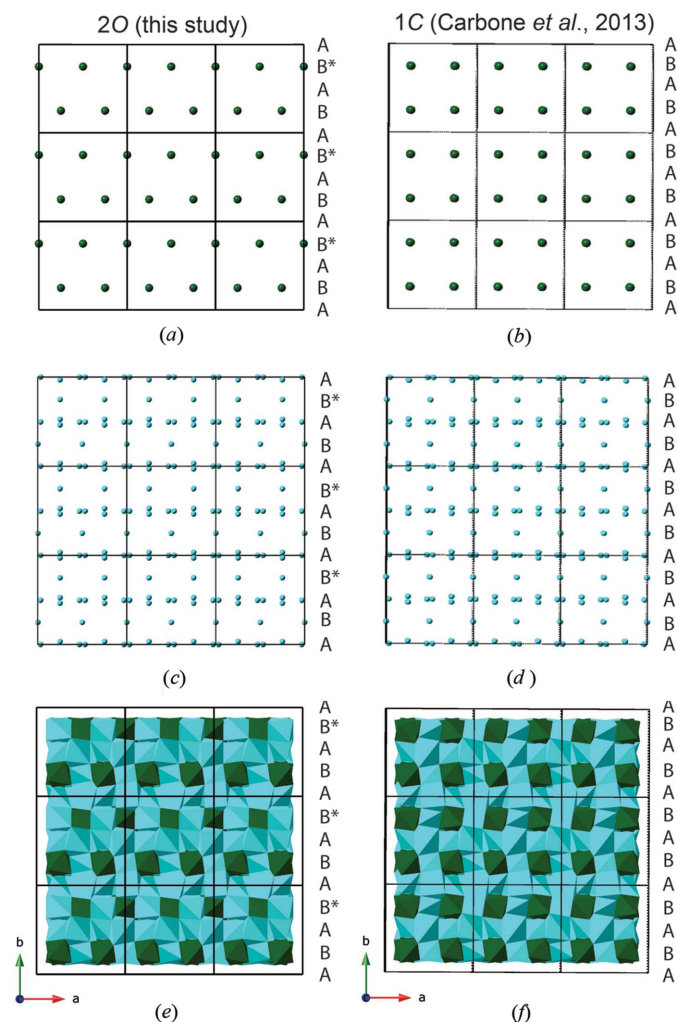
Figure 7
Crystal structure comparison of $Cu^{II}_3Te^{VI}O_6$-2*O* and $Cu^{II}_3Te^{VI}O_6$-1*C* comparing Te sites (*a* and *b*), Cu (*c* and *d*) and overall octahedral stacking (*e* and *f*). Te shown in dark green and Cu in light blue, drawn using *Crystalmaker* (Palmer, 2009).
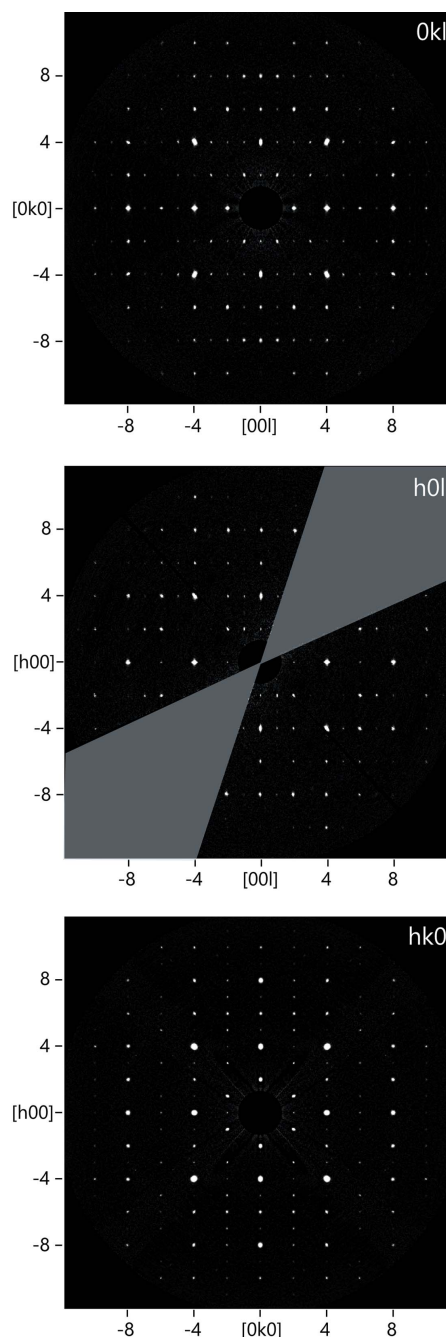

Figure 8
Reconstructed main zones from the 3D ED analysis of $Cu^{II}_3Te^{VI}O_6$-2*O*; the missing fraction of reciprocal space is highlighted in grey.

$Cu^{II}O_6$ octahedra in every second layer giving an $ABAB*$ stacking arrangement.

As a result of the lower symmetry, a larger number of unique crystallographic sites are present in the crystal structure of $Cu^{II}_3Te^{VI}O_6$-$2O$, namely five Cu (4a, 1; 4c, .2.; 4e, ..2; 4e, ..2; 4c, .2.), two Te (4b, 1; 4d, ..2) and six O sites (all on 8f, 1) (Fig. 9). A greater range of bond lengths compared to the $1C$ polytype is also observed to accommodate the stacking offset, with up to 0.13 Å of variation observed for Cu—O bonds and up to a 0.18 Å increase in bond length for Te—O bonds observed in the 3D ED refinement. The average Cu—O equatorial bond length in $Cu^{II}_3Te^{VI}O_6$-$2O$ is 2.025 Å and the Cu—O axial bond length is 2.425 Å. The Te1O$_6$ octahedron is close to symmetrical (Mills & Christy, 2013), with all bonds between 1.969 (14) Å and 1.988 (15) Å, whereas the Te2O$_6$ octahedron is more distorted, with 2 × Te2—O6 bonds at
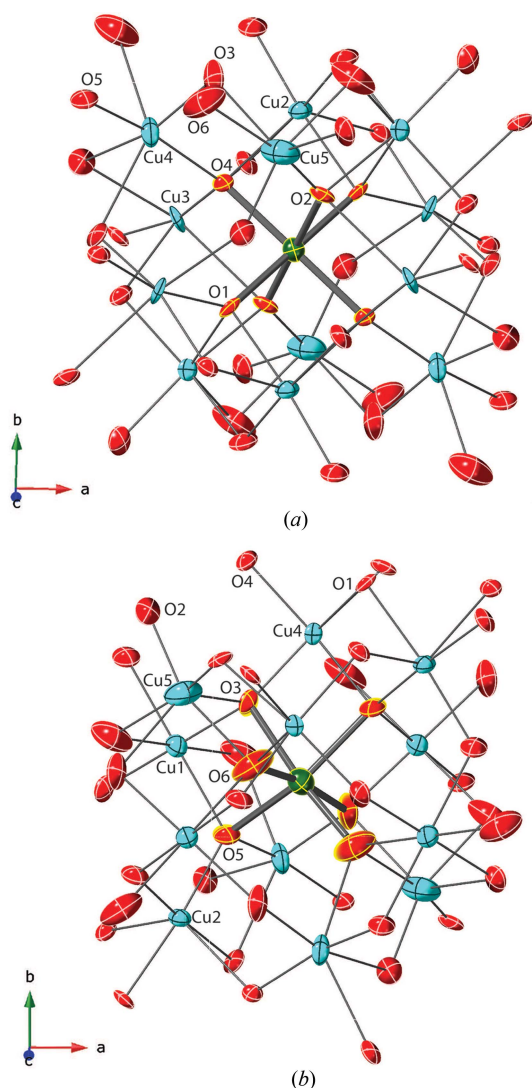
Table 4
Atomic coordinates and displacement parameters for $Cu^{II}_3Te^{VI}O_6$-$2O$ refined from 3D ED (regular text) and Rietveld (italic, shown for refined values) refinement.

Atom	x/a	y/b	z/c	U_{eq}
Cu1	$\frac{1}{2}$	1	$\frac{1}{2}$	0.0239 (14)
				0.01011 (19)
Cu2	$\frac{1}{2}$	0.7169 (8)	$\frac{1}{4}$	0.0356 (18)
		0.7205 (5)		*0.01011 (19)*
Cu3	$\frac{3}{4}$	$\frac{1}{2}$	0.2166 (9)	0.028 (2)
			0.2180 (3)	*0.01011 (19)*
Cu4	0.2191 (5)	0.7482 (6)	0.5046 (10)	0.020 (2)
	0.2157 (3)	*0.7484 (4)*	*0.4998 (3)*	*0.01011 (19)*
Cu5	$\frac{1}{2}$	0.2208 (11)	$\frac{1}{4}$	0.021 (2)
		0.2244 (5)		*0.01011 (19)*
Te1	$\frac{1}{2}$	$\frac{1}{2}$	$\frac{1}{2}$	0.0355 (17)
				0.0112 (8)
Te2	$\frac{3}{4}$	0	0.3028 (6)	0.044 (4)
			0.30388 (17)	*0.0159 (8)*
O1	0.6189 (14)	0.5762 (14)	0.3532 (17)	0.022 (4)
	0.6176 (14)	*0.5795 (15)*	*0.3482 (12)*	*0.01011 (19)*
O2	0.4304 (16)	0.3500 (15)	0.3824 (19)	0.030 (5)
	0.4254 (16)	*0.3544 (11)*	*0.3857 (15)*	*0.01011 (19)*
O3	0.3546 (16)	0.8778 (18)	0.5641 (18)	0.034 (6)
	0.3623 (13)	*0.8642 (12)*	*0.5666 (15)*	*0.01011 (19)*
O4	0.3555 (15)	0.6174 (14)	0.4220 (17)	0.023 (5)
	0.33984	*0.6067 (11)*	*0.4283 (14)*	*0.01011 (19)*
O5	0.4000 (17)	0.8580 (15)	0.140 (2)	0.033 (6)
	0.3965 (15)	*0.85823*	*0.1547 (11)*	*0.01011 (19)*
O6	0.643 (2)	0.091 (2)	0.169 (2)	0.055 (8)
	0.6298 (14)	*0.0906 (13)*	*0.1614 (12)*	*0.01011 (19)*

1.90 (2) Å, 2 × Te2—O3 bonds at 2.037 (18) Å and 2 × Te2—O5 bonds at 2.089 (16) Å (Fig. 9). Te1O$_6$ octahedra and Cu2O$_6$ octahedra are found in one {Cu–Te–O} layer and Te2O$_6$ octahedra and Cu3O$_6$ octahedra in the other. The remaining three CuO$_6$ octahedra (Cu1, Cu4 and Cu5) are found in the alternating {Cu–O} layers.

3.2. Rietveld refinement of $Cu^{II}_3Te^{VI}O_6$-$2O$

The unit-cell parameters of $Cu^{II}_3Te^{VI}O_6$-$2O$ from the Rietveld refinement [a = 9.56157 (19) Å, b = 9.55853 (11) Å and c = 9.62891 (15) Å] are ~1.5% lower than those determined by 3D ED, well within the 3% error typically assumed for 3D ED measurements of this nature. The experimental powder pattern presents an anisotropic peak shape which results from anisotropic crystallite size, which was treated using spherical harmonics. To be able to estimate the average crystallite size and shape, the instrumental contribution was evaluated using a silicon reference sample. The average crystallite topology can be represented by a elongated plate-like shape formed from two smaller fused crystallites, with estimated dimensions 20 × 13.5 × 64.5 nm along the main crystallographic directions (Fig. 10).

The structure derived from the Rietveld refinement is similar to that determined from 3D ED, with the most notable difference observed for the Cu1 site. In the 3D ED refinement, the two Cu1—O5 bonds are equatorial 2.177 (17) Å and Cu1—O6 bonds are axial 2.34 (2) Å, whereas in the Rietveld refinement the Cu1—O6 bonds are shorter than the Cu1—O5 bonds, 2.169 (13) and 2.244 (10) Å respectively. The smaller

Figure 9
Crystal structure of $Cu^{II}_3Te^{VI}O_6$-$2O$ showing local bonding environments around (a) Te1 and (b) Te2. Colour scheme as above with O atoms in red, with the six Te—O bonds shown as thick cylinders and these O atoms in yellow highlight. Ellipsoids shown at the 50% probability level, drawn using *Crystalmaker* (Palmer, 2009).

unit-cell in the Rietveld refinement also leads to shorter Cu—O bonds on average compared to the 3D ED refinement, with an average 1.977 Å axial bond length and 2.380 Å equatorial bond length, compared to 2.025 and 2.425 Å for the 3D ED refinement, respectively. This leads to higher bond-valence sums for the Cu^{II} sites, 2.10 compared to 1.83 valence units. Despite these bond-length differences, the topology of the structures as determined from the two techniques is near identical (see comparisons in Tables 4, 5 and 6).

3.3. Group–subgroup relationship

The structural relationship between the bixbyite-type $Cu^{II}_3Te^{VI}O_6$-$1C$ aristotype and the $Cu^{II}_3Te^{VI}O_6$-$2O$ hettotype can be concisely expressed by using a 'Bärnighausen family tree' (Bärnighausen, 1980; Müller, 2004, 2017). Corresponding relationships between Wyckoff positions and coordinates were
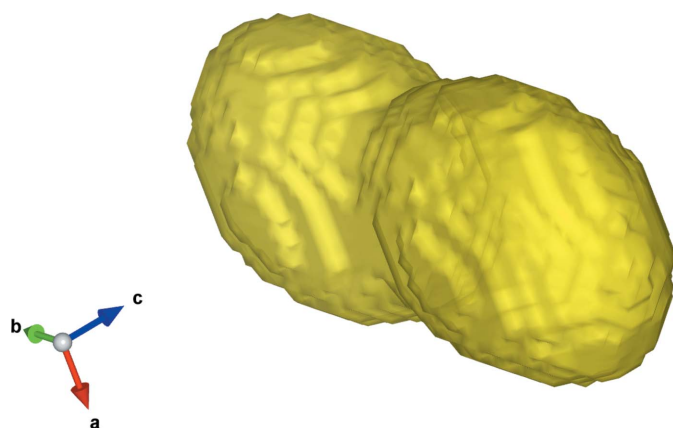

Figure 10
Visualization of the average crystallite size (20 × 13.5 × 64.5 nm) and shape as obtained from the Rietveld refinement shown in Fig. 4. The elongated shape of the average crystallite explains the anisotropic peak shape in the experimental powder pattern.

checked and derived with the aid of the program *WYCKS-PLIT* (Kroumova *et al.*, 1998) available at the Bilbao Crystallographic Server (Aroyo *et al.*, 2006).

There is no direct relation between the cubic $Cu^{II}_3Te^{VI}O_6$-$1C$ structure ($Ia\bar{3}$, No. 206, Z = 8) and the orthorhombic $Cu^{II}_3Te^{VI}O_6$-$2O$ (*Pcca*, No. 54, Z = 8) structure. Hence, a hypothetical *I*-centred intermediate orthorhombic structure with similar unit-cell parameters (a, b, c ≃ 9.6 Å) in space group *Ibca* (No 73, Z = 8) is needed (Fig. 11). The symmetry reduction from the $Cu^{II}_3Te^{VI}O_6$-$1C$ aristotype to the hypothetical structure in space group *Ibca* is of the *translationengleiche* type with index 3 (t3), whereas the symmetry reduction from *Ibca* to the $Cu^{II}_3Te^{VI}O_6$-$2O$ hettotype is of the *klassengleiche* type with index 2 (k2).

As can be seen in Fig. 11, the Cu2 and Te1 sites of the hypothetical structure in *Ibca* each split into one Cu and one Te site in the $Cu^{II}_3Te^{VI}O_6$-$2O$ structure that give rise to the assumption that sites Cu2 and Te1 in the hypothetical structure each could be statistically occupied by the two types of elements. Although the coordination spheres around Cu^{II} and Te^{VI} usually are distinctly different due to the Jahn–Teller distortion of Cu^{II}, examples for mixed occupation of Cu and Te on the same site are known, *e.g.* in the monoclinic form of $PbCuTeO_5$ (Weil *et al.*, 2019). The symmetry relationships between $Cu^{II}_3Te^{VI}O_6$-$1C$ and $Cu^{II}_3Te^{VI}O_6$-$2O$ (including a hypothetical intermediate structure) make it obvious that a direct structural transformation of $Cu^{II}_3Te^{VI}O_6$-$1C$ into $Cu^{II}_3Te^{VI}O_6$-$2O$ and vice versa is not possible because this requires a complete reorganization of some of the Cu and Te positions.

As shown, the group–subgroup relationship between the cubic aristotype and the orthorhombic hettotype of $Cu^{II}_3Te^{VI}O_6$ requires an intermediate hypothetical structure. However, this does not rule out that other crystal structures for phases with composition $Cu^{II}_3Te^{VI}O_6$ also could exist, *e.g.* with a different stacking arrangement or with stacking faults of the A,B layers.
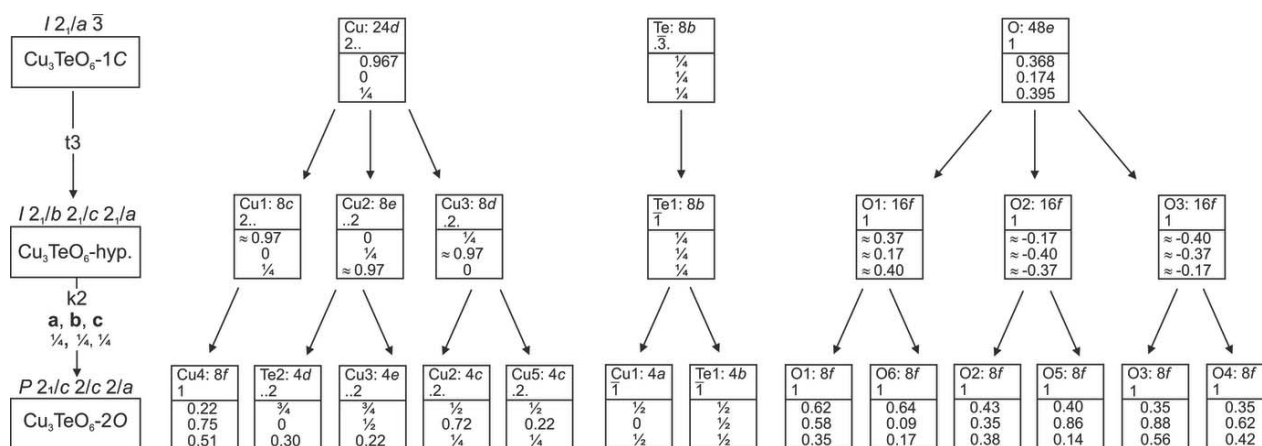

Figure 11
Bärnighausen family tree showing the group–subgroup relationships between the bixbyite-type cubic aristotype structure of $Cu^{II}_3Te^{VI}O_6$-$1C$, a hypothetical intermediate structure and the orthorhombic hettotype structure of $Cu^{II}_3Te^{VI}O_6$-$2O$. Atomic coordinates of $Cu^{II}_3Te^{VI}O_6$-$1C$ were taken from Falck *et al.* (1978), atomic coordinates of $Cu^{II}_3Te^{VI}O_6$-$2O$ from the current refinement.

3.4. Further observations

XRPD scans of all the natural $Cu^{II}_3Te^{VI}O_6$ samples analysed in this study revealed them to be $Cu^{II}_3Te^{VI}O_6$-$2O$, sometimes with extra minor reflections, probably from other minerals incorporated as microinclusions in the $Cu^{II}_3Te^{VI}O_6$ coatings. The vast majority of low-temperature hydrothermal syntheses produced $Cu^{II}_3Te^{VI}O_6$-$2O$, with the exception of two evaporative hydrothermal syntheses, which produced $Cu^{II}_3Te^{VI}O_6$-$1C$. $Cu^{II}_3Te^{VI}O_6$-$2O$ was the only product in several syntheses using Cu:Te ratios of 6:1, with excess Cu^{II} seemingly remaining soluble and no additional phases detected in the powder X-ray diffraction patterns. The lack of competing products co-crystallizing in the second batch of experiments led to greater purity of products, even following washing to remove soluble phases. These observations allow the following conclusions to be drawn: (1) mild hydrothermal conditions favour the formation of $Cu^{II}_3Te^{VI}O_6$-$2O$, especially when water remains in the system and (2) rapid evaporation of the solvent may promote the formation of $Cu^{II}_3Te^{VI}O_6$-$1C$ at temperatures below 473 K, providing one explanation for the possible formation of $Cu^{II}_3Te^{VI}O_6$-$1C$ from the Gambatesa mine (Carbone *et al.*, 2013). Analysis of the data presented by Carbone *et al.* (2013) shows that, at the very least, their natural $Cu^{II}_3Te^{VI}O_6$-$1C$ was intermixed with $Cu^{II}_3Te^{VI}O_6$-$2O$. For instance, Carbone *et al.* (2013) present a Raman spectrum for mcalpineite with a broad double maximum (as determined for $Cu^{II}_3Te^{VI}O_6$-$2O$ in this study) and noted a *d*-spacing at 4.25 Å in their ED experiment from an 'impurity' phase. This 4.25 Å *d*-spacing is present in all $Cu^{II}_3Te^{VI}O_6$-$2O$ XRPD scans but is not observed for the $1C$ polytype.

Conversion from $Cu^{II}_3Te^{VI}O_6$-$1C$ to $Cu^{II}_3Te^{VI}O_6$-$2O$ does not readily occur. A sample of $Cu^{II}_3Te^{VI}O_6$-$1C$ was heated at 473 K under hydrothermal conditions for five days, after which the powder diffraction pattern showed no changes, even though these conditions produce $Cu^{II}_3Te^{VI}O_6$-$2O$ when synthesized directly from Cu^{II} and Te^{VI} sources (as discussed).

3.5. Raman and IR spectroscopy

The dominant feature of all IR and Raman spectra relates to the Te—O stretching band(s). The Raman spectrum of $Cu^{II}_3Te^{VI}O_6$-$2O$ features a broad, strong double maximum with bands at 693 and 741 cm^{-1}, whereas the spectrum of CVT-generated crystals of $Cu^{II}_3Te^{VI}O_6$-$1C$ contains a single strong maximum centred on 730 cm^{-1}. The broad double maximum is likely related to the lower symmetry of the $Cu^{II}_3Te^{VI}O_6$-$2O$ polytype, which contains a range of Te—O bond lengths rather than the single Te—O bond length in $Cu^{II}_3Te^{VI}O_6$-$1C$. The higher fidelity of the spectrum collected on $Cu^{II}_3Te^{VI}O_6$-$1C$ shows many smaller bands which are not discernible for $Cu^{II}_3Te^{VI}O_6$-$2O$, although more bands between 200 and 500 cm^{-1} might be expected if a higher signal to noise ratio were achieved. The bands at 674, 655, 621 and 545 cm^{-1} are likely to be related to less prominent stretching vibrations (including antisymmetric stretching) of Te—O bonds, while those below 500 cm^{-1} are expected to be related to Cu—O modes and symmetric and antisymmetric Te—O bending modes. The Raman spectrum of mcalpineite from Bird Nest drift shows a marked similarity to $Cu^{II}_3Te^{VI}O_6$-$2O$, with a broad double maximum related to the Te—O stretching modes. The bands for this feature are at 696 and 743 cm^{-1}, within 5 cm^{-1} of the bands generated by synthetic $Cu^{II}_3Te^{VI}O_6$-$2O$. Mcalpineite from the Gambatesa mine (Carbone *et al.*, 2013) also shows the double maximum bands, again indicating the presence of $Cu^{II}_3Te^{VI}O_6$-$2O$ from this locality rather than only $Cu^{II}_3Te^{VI}O_6$-$1C$. No features were observed between 4000 and 1100 cm^{-1} in the Raman spectra for either polytype of $Cu^{II}_3Te^{VI}O_6$ (natural or synthetic).

Scans on $Cu^{II}_3Te^{VI}O_6$-$1C$ whether produced by solid-state synthesis or CVT have near-identical IR spectra. However, unlike the Raman spectra, the IR spectra show significant variation when comparing $Cu^{II}_3Te^{VI}O_6$-$2O$ to $Cu^{II}_3Te^{VI}O_6$-$1C$ between 4000 and 1600 cm^{-1}. $Cu^{II}_3Te^{VI}O_6$-$1C$ shows no significant features in this region (spectra have minor oscillation, but no bands), but $Cu^{II}_3Te^{VI}O_6$-$2O$ has a moderately strong, broad absorbance centred on ~3380 cm^{-1} and a weak mode at ~1639 cm^{-1}. Although these bands are characteristic of the stretching and bending modes, respectively, of H_2O, there are no cavities within $Cu^{II}_3Te^{VI}O_6$-$2O$ suitable for the presence of structural H_2O. It is thus most likely that the water is adsorbed on the surface of $Cu^{II}_3Te^{VI}O_6$-$2O$ granules, resulting in broad bands due to ill-defined water environments. In the region between 1000 and 370 cm^{-1}, each IR spectrum contains five bands, three in the Te—O stretching region and two in the Te—O bending region. The three stretching region band positions are strong, sharp and near-identical for the two $Cu^{II}_3Te^{VI}O_6$-$1C$ samples (CVT bands at 706, 673 and 638 cm^{-1}; solid-state spectrum has bands within
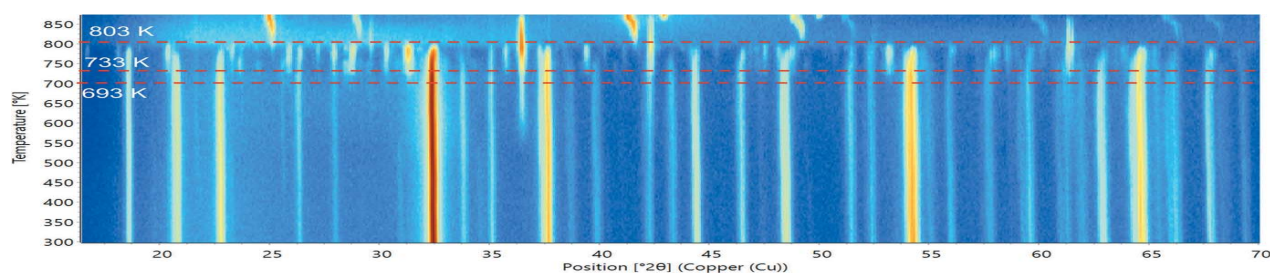
Figure 12
Temperature-dependent XRPD scans of synthetic $Cu^{II}_3Te^{VI}O_6$-$2O$, with temperature (K) on the vertical axis plotted against 2θ (°) on the horizontal axis. Phase transitions are marked with red lines.

Table 5
Selected bond lengths (in Å) for $Cu^{II}_3Te^{VI}O_6$-$2O$ as determined by 3D ED (regular text) and Rietveld (in italics) refinement.

	3D ED	Rietveld		3D ED	Rietveld
Cu1—O3 (×2)	1.954 (17)	*1.957 (13)*	Cu5—O2 (×2)	1.929 (18)	*1.939 (14)*
Cu1—O5 (×2)	2.177 (17)	*2.244 (10)*	Cu5—O6 (×2)	2.04 (2)	*1.976 (14)*
Cu1—O6 (×2)	2.34 (2)	*2.169 (13)*	Cu5—O3 (×2)	2.496 (17)	*2.360 (14)*
$\langle Cu1-O \rangle_{short}$	2.066	*2.063*	$\langle Cu5-O \rangle_{short}$	1.986	*1.958*
$\langle Cu1-O \rangle_{long}$	2.336	*2.244*	$\langle Cu5-O \rangle_{long}$	2.496	*2.360*
Cu2—O5 (×2)	2.002 (18)	*1.885 (10)*	Te1—O4 (×2)	1.969 (14)	*1.965 (8)*
Cu2—O1 (×2)	2.059 (15)	*1.994 (14)*	Te1—O2 (×2)	1.979 (16)	*1.912 (13)*
Cu2—O4 (×2)	2.398 (16)	*2.545 (16)*	Te1—O1 (×2)	1.988 (15)	*1.995 (13)*
$\langle Cu2-O \rangle_{short}$	2.031	*1.940*	$\langle Te1-O \rangle$	1.979	*1.957*
$\langle Cu2-O \rangle_{long}$	2.398	*2.545*			
			Te2—O6 (×2)	1.90 (2)	*1.988 (13)*
Cu3—O1 (×2)	1.991 (16)	*1.937 (13)*	Te2—O3 (×2)	2.037 (18)	*2.096 (13)*
Cu3—O4 (×2)	2.050 (16)	*1.940 (12)*	Te2—O5 (×2)	2.089 (16)	*1.989 (11)*
Cu3—O2 (×2)	2.483 (16)	*2.397 (14)*	$\langle Te2-O \rangle$	2.009	*2.024*
$\langle Cu3-O \rangle_{short}$	2.021	*1.939*			
$\langle Cu3-O \rangle_{long}$	2.483	*2.397*			
Cu4—O3	1.918 (18)	*1.898 (13)*			
Cu4—O4	2.011 (16)	*1.928 (10)*			
Cu4—O5	2.060 (19)	*2.116 (11)*			
Cu4—O2	2.113 (18)	*1.998 (15)*			
Cu4—O1	2.387 (16)	*2.372 (14)*			
Cu4—O6	2.43 (2)	*2.335 (13)*			
$\langle Cu4-O \rangle_{short}$	2.026	*1.985*			
$\langle Cu4-O \rangle_{long}$	2.407	*2.394*			

5 cm^{-1} of these values) and a higher-energy triplicate peak for $Cu^{II}_3Te^{VI}O_6$-$2O$ (665, 634 and 592 cm^{-1}). All of the IR spectra have small absorbance bands between 2000 and 2500 cm^{-1} (resulting from absorption of the used ATR diamond), but no components of $Cu^{II}_3Te^{VI}O_6$ would be expected to produce bands in this region.

3.6. Thermal analysis

Thermogravimetric analysis suggested the loss of ~1.8% mass from the sample of synthetic $Cu^{II}_3Te^{VI}O_6$-$2O$ used in the analysis, though this mass loss is less than 50% of what would be required for stoichiometric loss of one H_2O molecule per formula unit (*e.g.* 4.2% mass loss for theoretical Cu^{II}_3-$Te^{VI}O_6 \cdot H_2O$). Based on structural and IR considerations, it is most likely that the water associated with the mass loss was adsorbed, rather than structural. $Cu^{II}_3Te^{VI}O_6$-$2O$ decomposes in a series of steps (Fig. 12). DSC revealed several transformations as $Cu^{II}_3Te^{VI}O_6$-$2O$ is heated (Fig. 13). A small exothermic event is followed by an endothermic event centred on 673 K, without any obvious XRPD changes. The powder pattern remains virtually constant up until 728 K when new reflections start to become visible, although an exothermic change begins to occur earlier (at 693 K) and continues until 733 K (Fig. 12). New phases to develop between 728 K and 803 K include Cu_2O (ICDD code 04-007-9767) and orthorhombic $CuTeO_3$ (balyakinite, 01-071-2230). Their formation is an exothermic process. Thermodynamically, following the exothermic change, no significant feature occurs until 763 K, when endothermic change occurs until 803 K (Fig. 13). Above 808 K, Cu_2O is dominant, and is found along with cubic Cu_2Te (01-082-4898; 01-082-4898). A final XRPD scan was collected

following cooling back to 303 K, showing hexagonal Cu_2Te (weissite, 04-019-1996) without any evidence of Cu_2O. The decomposition of $Cu^{II}_3Te^{VI}O_6$-$2O$ may proceed by the following two-step process, although it is worth noting that amorphous Cu–Te–O phases may also constitute some of the high-temperature decomposition products, potentially lowering the amount of O released during the decomposition:
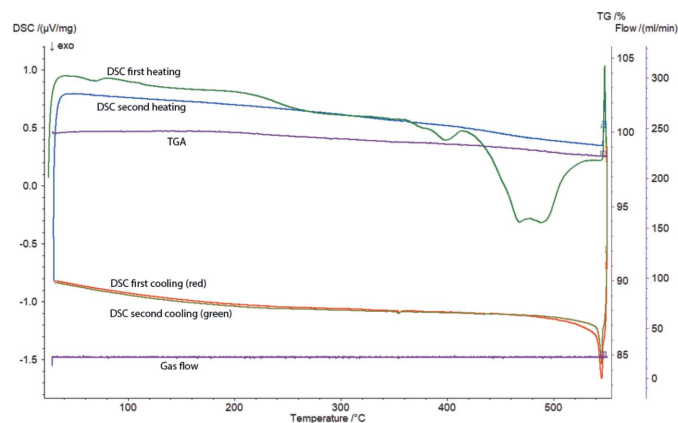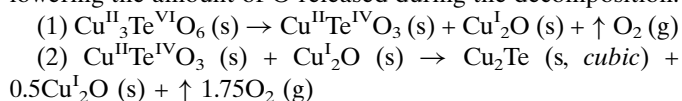
(1) $Cu^{II}_3Te^{VI}O_6$ (s) → $Cu^{II}Te^{IV}O_3$ (s) + Cu^I_2O (s) + ↑ O_2 (g)

(2) $Cu^{II}Te^{IV}O_3$ (s) + Cu^I_2O (s) → Cu_2Te (s, *cubic*) + $0.5Cu^I_2O$ (s) + ↑ $1.75O_2$ (g)

Figure 13
TGA and DSC traces of synthetic $Cu^{II}_3Te^{VI}O_6$-$2O$. TGA trace is in purple. Two cycles of DSC begin with the bright-green line (first heating), red line (first cooling), blue line (second heating), dull-green line near overlying the red line (second cooling).

Table 6
Bond valences for $Cu^{II}_3Te^{VI}O_6$-$2O$ using bond lengths from the 3D ED refinement.

Sums for Rietveld are also shown in the table in italics. Bond-valence parameters taken from Gagné & Hawthorne (2015) for Cu—O bonds and Mills & Christy (2013) for Te^{VI}—O bonds.

Atom	Cu1	Cu2	Cu3	Cu4	Cu5	Te1	Te2	Σ_{ED}	$\Sigma_{Rietveld}$
O1		0.35 (×2↓)	0.42 (×2↓)	0.14		0.89(×2↓)		1.80	*1.94*
O2			0.11 (×2↓)	0.30	0.51 (×2↓)	0.92 (×2↓)		1.83	*1.97*
O3	0.47 (×2↓)			0.52	0.10 (×2↓)		0.81 (×2↓)	1.91	*1.90*
O4		0.13 (×2↓)	0.36 (×2↓)	0.40		0.90 (×2↓)		1.80	*2.10*
O5	0.25 (×2↓)	0.41 (×2↓)		0.35			0.74 (×2↓)	1.75	*1.97*
O6	0.16 (×2↓)			0.12	0.37 (×2↓)		1.04 (×2↓)	1.69	*1.75*
Σ_{ED}	1.76	1.79	1.78	1.84	1.96	5.41	5.18		
$\Sigma_{Rietveld}$	*1.87*	*2.17*	*2.24*	*2.08*	*2.17*	*5.63*	*5.01*		

3.7. Observations in the Cu^{II}–Te^{VI}–O–H $\pm$ system

$Cu^{II}_3Te^{VI}O_6$ is highly stable across a wide range of conditions and with a wide variety of other compounds. $Cu^{II}_3Te^{VI}O_6$ was hydrothermally synthesized across a pH range of 0 to 14 and was encountered (not necessarily in a pure form) with a wide variety of counter-cations and counter-anions, including Na^+, K^+, Ag^+, Pb^{2+}, CO_3^{2-}, NO_3^-, SO_4^{2-} and Cl^-.

Additional impure samples of $Cu^{II}_3Te^{VI}O_6$ were also generated from syntheses initially incorporating TeO_2. Oxidation of Te^{IV} in TeO_2 to Te^{VI} occurred in both high-temperature solid-state syntheses and in hydrothermal syntheses in which dehydration occurred, but never in hydrothermal syntheses in which water remained. Oxidation presumably occurred with atmospheric oxygen as the oxidant.

3.8. $Cu^{II}_3Te^{VI}O_6$ as a sink for other cations

The results of the EPMA analysis of Millsite Boulder mcalpineite from Norway are (oxide, average, min–max, standard deviation): Cu (CuO, 45.40, 41.53–48.77, 2.3), Te (TeO$_3$, 41.51, 40.87–42.52, 0.6) and U (UO$_2$, 9.62, 6.62–12.90, 2.1). The data lead to a somewhat low analytical total of 96.54 wt%, attributed to the heterogeneous nature of the mcalpineite (porous and formed from crystals <1 μm in size). The empirical formula is $Cu_{2.53}U_{0.16}Te_{1.05}O_{6.00}$ and the simplified formula is $(Cu^{II}_{2.53}U^{IV}_{0.16}Te^{VI}_{0.11})_{\Sigma 2.80}Te^{VI}_{0.94}O_6$, based on six O anions per formula unit, showing >5 at% U^{IV} substitution of Cu^{II} compared to the ideal formula, Cu^{II}_3-$Te^{VI}O_6$. It is worth noting that this substitution requires vacancies in the crystal structure to maintain charge balance, though less vacancies than if U^{VI} were to substitute for Cu^{II}. We postulate that the U^{IV} is able to substitute for Cu^{II} as Jahn–Teller distorted Cu^{II} cations (average Cu—O bond length in mcalpineite-$2O$ 2.111 Å) provide more space for the larger U^{IV} cations than regular Te^{VI} octahedra (Te—O average 1.991 Å). While Te^{VI}–U^{VI} substitution has been observed in the mineral markcooperite ($PbUO_2Te^{VI}O_6$), which has a mixed U^{VI}:Te^{VI} site in a 75:25% ratio (Kampf et al., 2010), the EPMA data suggest that U^{IV} substitutes for Cu^{II} in this case.

These results indicate that mcalpineite might be a sink for U in Cu- and Te-rich weathering zones, an observation that may have significance in the area of nuclear remediation. Radioactive isotopes of Te including ^{132}Te and $^{129\,m}$Te are released by nuclear fission, meaning that these isotopes must be accounted for in remediation of sites such as Fukushima Dai-ichi following the nuclear power plant disaster in 2011 (Dickson & Glowa, 2019; Tagami et al., 2013; Takahashi et al., 2019). U-bearing mcalpineite could be used to entrap both Te and U due to its high stability over the full pH range (as shown by our syntheses of $Cu^{II}_3Te^{VI}O_6$) and its ability to incorporate both elements. $Cu^{II}_3Te^{VI}O_6$ may also incorporate other cations into its structure, including Zn (5 at% substitution for Cu, Centennial Eureka Mine; Roberts et al., 1994) and Pb (3 at% substitution for Cu at McAlpine mine; Roberts et al., 1994) in cotype material. Incorporation of Pb into mcalpineite appears to be relatively common, with 3 at% Pb substitution for Cu observed in mcalpineite from Delamar and 6 at% Pb from Otto Mountain in SEM in this study, showing the versatility of the $Cu^{II}_3Te^{VI}O_6$-$2O$ structure. Future studies should quantify the ability of mcalpineite to incorporate different cations.

3.9. Cu_3TeO_6 polytypes in Nature

The mineral mcalpineite consists of two polytypes of $Cu^{II}_3Te^{VI}O_6$, with the entirety of the North American specimens, all collected from weathering zone Te–O mineral assemblages, consisting of mcalpineite-$2O$. The only localities where pure mcalpineite-$1C$ is likely to be formed naturally are high-temperature oxidizing fumaroles (as opposed to the apparent mixture of mcalpineite polytypes at the weathering zone of the Gambatesa mine, Italy). Mcalpineite has been reported from one fumarole to date (Pekov et al., 2019), the Arsenatnaya fumarole, Second scoria cone, Tolbachik Volcano, Kamchatka Krai, Russia (55.68333°N, 160.23333°E; Pekov et al., 2018). Mcalpineite was found in amounts insufficient for collecting a powder X-ray diffraction scan (Pekov et al., 2019). It is likely that this mcalpineite is mcalpineite-$1C$, pending future confirmation by either XRPD or Raman spectroscopy.

research papers

References

Aroyo, M. I., Perez-Mato, J. M., Capillas, C., Kroumova, E., Ivantchev, S., Madariaga, G., Kirov, A. & Wondratschek, H. (2006). *Z. Kristallogr.* **221**, 15–27.

Atencio, D., Roberts, A. C., Matioli, P. A., Stirling, J. A. R., Venance, K. E., Doherty, W., Stanley, C. J., Rowe, R., Carpenter, G. J. C. & Coutinho, J. M. V. (2008). *Mineral. Mag.* **72**, 1201–1205.

Bärnighausen, H. (1980). *MATCH. Commun. Math. Chem.* **9**, 139–175.

Binnewies, M., Glaum, R., Schmidt, M. & Schmidt, P. (2012). *Chemical Vapor Transport Reactions*. DeGruyter, Berlin, Germany.

Carbone, C., Basso, R., Cabella, R., Martinelli, A., Grice, J. D. & Lucchetti, G. (2013). *Am. Mineral.* **98**, 1899–1905.

Chakraborty, J. (2019). *J. Phys. Chem. Solids*, **134**, 182–186.

Choi, K., Lemmens, P., Choi, E. & Berger, H. (2008). *J. Phys. Condens. Matter*, **20**, 505214.

Christy, A. G., Mills, S. J. & Kampf, A. R. (2016b). *Mineral. Mag.* **80**, 415–545.

Christy, A. G., Mills, S. J., Kampf, A. R., Housley, R. M., Thorne, B. & Marty, J. (2016a). *Mineral. Mag.* **80**, 291–310.

Dickson, R. S. & Glowa, G. A. (2019). *J. Environ. Radioact.* **204**, 49–65.

Falck, L., Lindqvist, O. & Moret, J. (1978). *Acta Cryst.* B**34**, 896–897.

Gagné, O. C. & Hawthorne, F. C. (2015). *Acta Cryst.* B**71**, 562–578.

Gemmi, M., Mugnaioli, E., Gorelik, T. E., Kolb, U., Palatinus, L., Boullay, P., Hovmöller, S. & Abrahams, J. P. (2019). *ACS Cent. Sci.* **5**, 1315–1329.

He, Z. & Itoh, M. (2014). *J. Magn. Magn. Mater.* **354**, 146–150.

Herak, M., Berger, H., Prester, M., Miljak, M., Živković, I., Milat, O., Drobac, D., Popović, S. & Zaharko, O. (2005). *J. Phys. Condens. Matter*, **17**, 7667–7679.

Hostachy, A. & Coing-Boyat, J. (1968). *C. R. Acad. Sci.* B**267**, 1435–1438.

Housley, R. M., Kampf, A. R., Mills, S. J., Marty, J. & Thorne, B. (2011). *Rocks Min.* **86**, 132–145.

Inosov, D. (2018). *Adv. Phys.* **67**, 149–252.

Kampf, A. R., Mills, S. J., Housley, R. M., Marty, J. & Thorne, B. (2010). *Am. Mineral.* **95**, 1554–1559.

Kolb, U., Gorelik, T., Kübel, C., Otten, M. & Hubert, D. (2007). *Ultramicroscopy*, **107**, 507–513.

Kroumova, E., Perez-Mato, J. M. & Aroyo, M. I. (1998). *J. Appl. Cryst.* **31**, 646–646.

Mills, S. J. & Christy, A. G. (2013). *Acta Cryst.* B**69**, 145–149.

Müller, U. (2004). *Z. Anorg. Allg. Chem.* **630**, 1519–1537.

Müller, U. (2017). *Symmetry Relationships between Crystal Structures*. Oxford University Press.

Mutharani, B., Rajakumaran, R., Chen, S.-M., Ranganathan, P., Chen, T.-W., Al Farraj, D. A., Ajmal Ali, M. & Al-Hemaid, F. M. A. (2020). *Microchem. J.* **159**, 105378.

Nénert, G., Missen, O. P., Lian, H., Weil, M., Blake, G. R., Kampf, A. R. & Mills, S. J. (2020). *Phys. Chem. Miner.* **47**, 1–8.

Norman, M. R. (2016). *Rev. Mod. Phys.* **88**, 041002.

Norman, M. R. (2018). *J. Magn. Magn. Mater.* **452**, 507–511.

Palatinus, L., Brázda, P., Jelínek, M., Hrdá, J., Steciuk, G. & Klementová, M. (2019). *Acta Cryst.* B**75**, 512–522.

Palatinus, L. & Chapuis, G. (2007). *J. Appl. Cryst.* **40**, 786–790.

Palmer, D. (2009). *CrystalMaker*. CrystalMaker Software Ltd. Yarnton, Oxfordshire, England.

Pekov, I. V., Chukanov, N. V., Zadov, A. E., Roberts, A. C., Jensen, M. C., Zubkova, N. V. & Nikischer, A. J. (2011). *Geol. Ore Depos.* **53**, 575–582.

Pekov, I. V., Koshlyakova, N. N., Zubkova, N. V., Lykova, I. S., Britvin, S. N., Yapaskurt, V. O., Agakhanov, A. A., Shchipalkina, N. V., Turchkova, A. G. & Sidorov, E. G. (2018). *Eur. J. Mineral.* **30**, 305–322.

Pekov, I. V., Turchkova, A. G., Yapaskurt, V. O., Sandalov, F. D. & Sidorov, E. G. (2019). *Miner. Divers. Res. Preserv. 10th Int. Symp.* pp. 63–66.

Petříček, V., Dušek, M. & Palatinus, L. (2014). *Z. Kristallogr.* **229**, 345–352.

Roberts, A. C., Ercit, T. S., Criddle, A. J., Jones, G. C., Williams, R. S., Cureton, F. F. II & Jensen, M. C. (1994). *Mineral. Mag.* **58**, 417–424.

Roberts, A. C., Gault, R. A., Jensen, M. C., Criddle, A. J. & Moffat, E. A. (1997). *Mineral. Mag.* **61**, 139–144.

Roberts, A. C., Grice, J. D., Criddle, A. J., Jensen, M. C., Harris, D. C. & Moffatt, E. A. (1995). *Can. Mineral.* **33**, 641–647.

Roberts, A. C., Grice, J. D., Groat, L. A., Criddle, A. J., Gault, R. A., Erd, R. C. & Moffatt, E. A. (1996a). *Can. Mineral.* **34**, 49–54.

Roberts, A. C., Groat, L. A., Grice, J. D., Gault, R. A., Jensen, M. C., Moffatt, E. A. & Stirling, J. A. (1996b). *Mineral. Mag.* **60**, 653–657.

Roberts, A. C., Stirling, J. A. R., Criddle, A. J., Jensen, M. C., Moffat, E. A. & Wilson, W. E. (1997). *Mineral. Rec.* **28**, 175.

Rumsey, M. S., Welch, M. D., Mo, F., Kleppe, A. K., Spratt, J., Kampf, A. R. & Raanes, M. P. (2018). *Mineral. Mag.* **82**, 433–444.

Spek, A. L. (2020). *Acta Cryst.* E**76**, 1–11.

Tagami, K., Uchida, S., Ishii, N. & Zheng, J. (2013). *Environ. Sci. Technol.* **47**, 5007–5012.

Takahashi, S., Kawashima, S., Hidaka, A., Tanaka, S. & Takahashi, T. (2019). *Nucl. Technol.* **205**, 646–654.

Wang, D., Bo, X., Tang, F. & Wan, X. (2019). *Phys. Rev. B*, **99**, 035160.

Weil, M., Shirkhanlou, M. & Stürzer, T. (2019). *Z. Anorg. Allg. Chem.* **645**, 347–353.

Williams, S. A. (1975). *Mineral. Mag.* **40**, 221–226.

Zhu, X., Wang, Z., Su, X. & Vilarinho, P. M. (2014). *Appl. Mater. Interfaces*, **6**, 11326–11332.